RESEARCH ARTICLE

Key Points:
- Dynamics of Langmuir turbulence as would be produced by auroral electron beams at the F region peak are investigated
- Suprathermal electrons, as modeled by Kappa distribution, have a significant effect on the development of Langmuir turbulence
- Wave products of three wave coalescence-like interactions may be intense enough to be detected by incoherent scatter radars

Correspondence to:
H. Akbari,
hakbari@bu.edu

Zakharov simulations of beam-induced turbulence in the auroral ionosphere

**H. Akbari[1], P. Guio[2], M. A. Hirsch[1], and J. L. Semeter[1]**

[1]Department of Electrical and Computer Engineering and Center for Space Physics, Boston University, Boston, Massachusetts, USA, [2]Department of Physics and Astronomy, University College London, London, UK

Abstract Recent detections of strong incoherent scatter radar echoes from the auroral F region, which have been explained as the signature of naturally produced Langmuir turbulence, have motivated us to revisit the topic of beam-generated Langmuir turbulence via simulation. Results from one-dimensional Zakharov simulations are used to study the interaction of ionospheric electron beams with the background plasma at the F region peak. A broad range of beam parameters extending by more than 2 orders of magnitude in average energy and electron number density is considered. A range of wave interaction processes, from a single parametric decay, to a cascade of parametric decays, to formation of stationary density cavities in the condensate region, and to direct collapse at the initial stages of turbulence, is observed as we increase the input energy to the system. The effect of suprathermal electrons, produced by collisional interactions of auroral electrons with the neutral atmosphere, on the dynamics of Langmuir turbulence is also investigated. It is seen that the enhanced Landau damping introduced by the suprathermal electrons significantly weakens the turbulence and truncates the cascade of parametric decays.

1. Introduction

Over the past few years, strong nonthermal echoes from the F region auroral ionosphere have been detected by various incoherent scatter radars (ISRs) [*Akbari et al.*, 2012, 2013; *Isham et al.*, 2012; *Ekeberg et al.*, 2012; *Schlatter et al.*, 2013, 2014]. The echoes that are often characterized by simultaneous enhancement of the received power in both the ion- and plasma-line channels thus, indicating simultaneous intensification of the ion-acoustic and Langmuir waves in the region of the ionosphere probed by the radar at wave vector imposed by the radar frequency and geometry, have been considered as signatures of naturally produced Langmuir turbulence. Furthermore, specific spectral features associated with the echoes, such as the presence of an additional peak at zero-Doppler in the ion-line spectra [*Isham et al.*, 2012] and double-peaked plasma-line spectra [*Akbari et al.*, 2012], have led to the conclusion that the turbulence proceeds toward the formation and collapse of cavitons. The observed features are similar to those detected during ionospheric modification (heating) experiments, where Langmuir turbulence is artificially generated in the ionosphere via injection of intense electromagnetic radiation by powerful high-frequency transmitters [*DuBois et al.*, 1990, 1993; *Stubbe et al.*, 1992; *Isham et al.*, 1999].

Correlating the ISR echoes with the optical measurements of aurora suggests that the auroral electron beams, in particular those generated by the parallel electric field of inertial Alfvenic waves [*Génot et al.*, 1999, 2004; *Bian and Kontar*, 2011; *Tsiklauri*, 2011, 2012], provide the free energy for the natural turbulence via a bump-on-tail instability. Beam-generated Langmuir turbulence has been the subject of experimental and simulation studies in many space environments, including the solar wind [*Nicholson et al.*, 1978], lower solar corona [*Goldman and Newman*, 1994], planetary foreshocks [*Gurnett et al.*, 1981; *Robinson and Newman*, 1991], and the topside auroral ionosphere [*Newman et al.*, 1994a, 1994b]. However, the development and dynamic of Langmuir turbulence are known to depend strongly on parameters of the background plasma, such as the level of background ion density perturbations, magnetic field, and kinetic effects such as damping rates for ion-acoustic and Langmuir waves, as well as the parameters of the source electron beam [*Newman et al.*, 1994a, 1994b; *Robinson et al.*, 1992; *Robinson and Newman*, 1989]. In the light of the ISR observations therefore it is valuable to conduct simulations that are representative of the plasma environments at the F region peak. Moreover, previous investigations of beam-generated Langmuir turbulence have all been based upon in situ measurements of waves with instruments onboard sounding rockets and satellites. ISR detections are much different from in situ measurements in that they indicate enhanced wave activities at a specific spatial scale, determined by the ISR probing wave number. This, in turn, puts additional requirements on
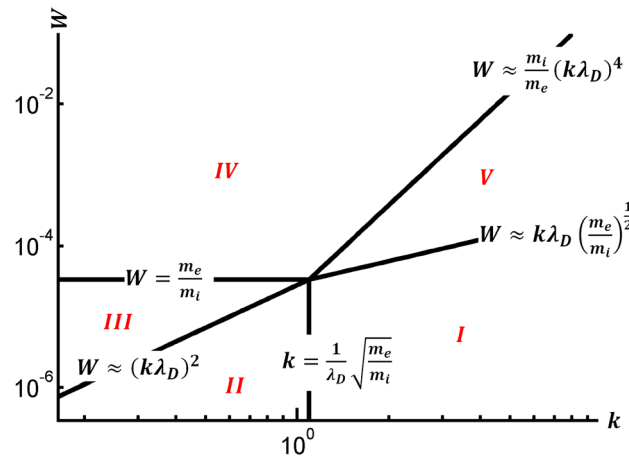
Figure 1. The five regimes of linear parametric instabilities for a monochromatic, plane Langmuir wave. The approximate boundaries are derived for the plasma parameters considered in this work. The five regions are (I) parametric decay instability, (II) modulational instability, (III) subsonic modulational instability, (IV) supersonic modulational instability, and (V) modified decay instability.

the characteristic energy of the electron beams and/or the dynamics of turbulence (for more context see *Akbari et al.* [2015]).

ISR observations of the echoes therefore motivated us to revisit the topic of beam-generated Langmuir turbulence in the *F* region ionosphere with the goal of reproducing the experimental observations and providing predictions of phenomenology to be investigated in future experiments. To this end we simulated Langmuir turbulence generated by electron beams with different set of parameters applicable to the *F* region ionosphere. The studied parameter regime was extended by more than 2 orders of magnitude in average energy and electron number density of the beams. The majority of the presented results correspond to the case where the bulk plasma distribution is considered Maxwellian. However, the effect of suprathermal (secondary) electrons, produced by the collisional interactions of the auroral electrons with the neutral atmosphere, and the associated enhanced Landau damping is also investigated through introducing an energetic tail to the bulk Maxwellian electrons in the form of a Kappa distribution.

2. Langmuir Turbulence

Langmuir turbulence occurs as a result of nonlinear interactions between Langmuir waves and ion density perturbations. In plasmas, the refractive index varies with plasma density, with lower density corresponding to higher refractive index. In the presence of Langmuir waves, an existing density depression therefore tends to refract the Langmuir energy inside. On the other hand, the electric field of Langmuir waves affects the low-frequency quasi-neutral plasma density perturbations through its ponderomotive force, which tends to push the plasma out of the regions of high electric field intensity. As a result of this positive feedback, instabilities emerge that lead to strong responses in the electric field and the density perturbations. Such interactions of Langmuir waves and plasma density perturbations are known to exist in a variety of natural and laboratory plasmas with vastly different parameters (over 23 orders of magnitude of plasma density, 4 orders of magnitude in electron temperature, and over 15 orders of magnitude in electric field amplitude [*Robinson*, 1997]).

Such interactions of Langmuir waves and ion density perturbations include the phenomena of linear parametric instabilities, as well as the completely nonlinear phenomenon of caviton formation and wave collapse. It was originally shown by *Zakharov et al.* [1985] that parametric instabilities of a monochromatic Langmuir wave in an isotropic and conservative plasma, i.e., neglecting collisional effects, are of five different types, each with their own thresholds, growth rates, and operating regimes on the intensity-wave number space. The five instabilities are (1) the parametric decay instability (PDI), (2) the modulational instability (MI), (3) the subsonic modulational instability, (4) the supersonic modulational instability, and (5) the modified decay instability. The applicability regimes of each of these instabilities are shown in Figure 1. In Figure 1, $W = \frac{\epsilon_0 |E|^2}{4 n_0 k_B T_e}$ (where E is the envelope of electric field, ϵ_0 is the permittivity of free space, n_0 is the electron density, k_B is the Boltzmann constant, and T_e is the electron temperature) is the ratio of the electrostatic energy to the plasma thermal energy. For detailed discussion of the instability regimes readers are referred to *Robinson* [1997] (a review paper).

As will be seen in section 3, for the background ionospheric plasma and beam parameters considered in this work, the initially enhanced Langmuir waves (due to the bump-on-tail instability) generally fall into the first region where the PDI is the dominant process. The parametric decay instability is a three-wave process during

which an initial intense Langmuir wave $L_1(\omega_{L1}, k_{L1})$ decays into a pair of product waves, including a secondary Langmuir wave $L_2(\omega_{L2}, k_{L2})$ and an ion-acoustic wave $S(\omega_s, k_s)$. With the dispersion relations of Langmuir and ion-acoustic waves, satisfying the frequency and wave number matching conditions–namely, $\omega_{L1} = \omega_{L2} + \omega_s$ and $k_{L1} = k_{L2} + k_s$—results in the following relations in one dimension: $k_{L2} = k^* - k_{L1}$ and $k_s \approx 2k_{L1} - k^*$ [e.g., *Forme*, 1993; *Diaz et al.*, 2010]. Here k is the wave number, $k^* = \frac{2}{3\lambda_D}\left(\eta \frac{m_e}{m_i}\right)^{\frac{1}{2}}$, $\eta = \frac{T_e + 3 T_i}{T_e}$, and m_e, m_i, λ_D, and T_i are the electron mass, ion mass, Debye length, and ion temperature, respectively. When $k_{L1} > k^*$, the above conditions imply that the product Langmuir wave propagates in the opposite direction of the initial wave (backscatter) and has a slightly smaller wave number. Provided that there is enough input energy to the system, the product Langmuir wave may grow to high intensities, decay, and create its own set of product waves in a similar fashion to the initial PDI. The process may further proceed in the form of a cascade of PDIs, transferring the energy to smaller wave numbers at each step, until the last produced Langmuir waves enter other regions of Figure 1 where modulational instabilities are the dominant process.

Modulational Instabilities are four-wave processes during which two Langmuir waves $L_1(\omega_{L1}, k_{L1})$ and L_2 $(\omega_{L2} = \omega_{L1}, k_{L2} = k_{L1})$ give rise to a pair of product Langmuir waves $L_3(\omega_{L3}, k_{L3} = k_{L1} - k_s)$ and $L_4(\omega_{L4}, k_{L4} = k_{L1} + k_s)$ via participation of an ion density perturbation $S(\omega_s, k_s)$. Depending on the regime of the instability, i.e., MI, subsonic MI, or supersonic MI: (1) the ion density perturbation can be an ion-acoustic wave or a strongly damped ion-acoustic quasi-mode and (2) k_s can be much larger or smaller than k_{L1}, i.e., Langmuir energy can transfer to higher or lower wave numbers [*Robinson*, 1997]. Modulational instabilities lead to the modulation of an initially uniform Langmuir wave and its break up into wave packets with scales $\sim k_s^{-1}$ [*Robinson*, 1997, and references therein], corresponding to the participating ion density perturbation. This breakup may sometimes be followed by a highly nonlinear stage where the wave packets progressively intensify and the density perturbations narrow and deepen (i.e., collapse to small scales) under the action of the ponderomotive force, forming localized density cavities with intense Langmuir energy trapped inside, i.e., cavitons.

In this report we intend to investigate the five instability regimes summarized in Figure 1 as well as formation of cavitons and revisit the topic of beam-generated Langmuir turbulence for the lower auroral ionosphere in the light of the new experimental data. In the next section we present the mathematical framework that is commonly used to simulate the Langmuir turbulence.

3. Zakharov Equations

Plasma at the peak of auroral F region, with electron cyclotron frequency of $f_c \approx 1.5$ MHz and plasma to cyclotron frequency ratio of $\frac{f_p}{f_c} \approx 4$, is weakly magnetized. Langmuir turbulence in such a plasma can be modeled by the electrostatic Zakharov equations [*DuBois et al.*, 1990; *Newman et al.*, 1994b].

Although, some aspects of Langmuir turbulence can only be truly captured in three-dimensional simulations [*Robinson*, 1997, and references therein], numerical works have shown that in many cases one-dimensional simulations are generally successful in representing the physics of the turbulence [e.g., *Rowland et al.*, 1981]. Moreover, in situ observations of beam-generated Langmuir turbulence in the topside auroral ionosphere have shown that the generated waves dominantly propagate with angles less than 10° with respect to the magnetic field lines [*Newman et al.*, 1994a]. This is in part due to the highly field-aligned nature of the source electron beams and in part due to the cyclotron damping for the waves propagating in oblique directions. In this work we restrict our attention to one-dimensional simulations since it enables a wider range of parameters to be studied in reasonable times. One-dimensional simulations, however, are not suitable at higher altitudes where the electron cyclotron frequency exceeds the plasma frequency [*Newman et al.*, 1994b].

In one dimension, the modified electrostatic Zakharov equations are given by [*Guio and Forme*, 2006]

$$\left(i\frac{\partial}{\partial t} + i\vartheta_e \times \ + \frac{3}{2}\omega_p \lambda_D^2 \frac{\partial^2}{\partial x^2}\right)E = \frac{\omega_p}{2}\frac{n}{n_0}E + S_E \tag{1}$$

$$\left(\frac{\partial^2}{\partial t^2} + 2\vartheta_i \times \frac{\partial}{\partial t} - C_s^2 \frac{\partial^2}{\partial x^2}\right)n = \frac{\epsilon_0}{4m_i}\frac{\partial^2 |E|^2}{\partial x^2} + S_n \tag{2}$$

where n is the low-frequency plasma density fluctuation and E is the slowly varying envelope of the high-frequency electric field (the total electrostatic field in terms of the slowly varying envelope is given

by $\mathscr{E} = \frac{1}{2}\left[E\exp(-i\omega_p t) + E^*\exp(i\omega_p t)\right]$). Other quantities are n_0, the background plasma density; $\omega_p = 2\pi f_p$, angular plasma frequency; $C_s = \frac{\eta m_e}{m_i}v_e^2$, the ion sound velocity; and $v_e^2 = \frac{k_B T_e}{m_e}$.

In the above equations, S_E and S_n are stochastic complex source terms that account for the thermal level emission of Langmuir and ion-acoustic waves. Landau and collisional damping are also accounted for by including appropriate damping coefficients $\vartheta_e = -\frac{\nu_{ec}}{2} + \gamma_L$ and $\vartheta_i = -\frac{\nu_{ic}}{2} + \gamma_s$, which include kinetically determined linear Landau damping of Langmuir and ion-acoustic waves (γ_L and γ_s, given by equations (3) and (4), respectively) and the effect of electron and ion collision frequencies (ν_{ec} and ν_{ic}, respectively) [*Guio and Forme*, 2006]. Note that the damping coefficients are wave number-dependent and are implemented in the Zakharov equations by incorporating the convolution product operator ×.

$$\gamma_L = \frac{\pi}{2n_0}\frac{\omega_p^2}{k^2}\omega_L\left[\frac{df(v)}{dv}\right]_{\omega_L/k} \tag{3}$$

$$\gamma_s = -\sqrt{\frac{\pi}{8}}\left[\left(\frac{m_e}{m_i}\right)^{\frac{1}{2}} + \left(\frac{T_e}{T_i}\right)^{\frac{3}{2}}\exp\left(-\frac{T_e}{2T_i}-\frac{3}{2}\right)\right]|k|C_s \tag{4}$$

In equation (3), $f(v)$ is the total one-dimensional electron distribution function which consists of the bulk ionospheric electrons, as well as the beam of electrons that provide the free energy for the turbulence via inverse Landau damping. The bulk and the electron beam populations are each modeled with Maxwellian distributions (equation (5)) with the proper choices of number density (n), mean velocity (u), and thermal velocity spread (θ).

$$f_{\text{Maxwellian}}(v) = \frac{n}{\theta\sqrt{2\pi}}\exp\left[-\frac{1}{2}\left(\frac{v-u}{\theta}\right)^2\right] \tag{5}$$

During periods of electron precipitation, such as the one we model here with a beam of electrons, an additional population of electrons with suprathermal energies (a few eV to ~ 100 eV), often called the secondary electrons [*Lummerzheim and Lilensten*, 1994] or the scattered electrons [*Newman et al.*, 1994b], emerges in the auroral ionosphere. This suprathermal population consists of an energetic tail, introducing a departure from the bulk Maxwellian distribution. Such departure will increase the Landau damping of Langmuir waves with phase velocity in the range of the modeled electron beam. Despite the significant effect of the secondary electrons on the dynamics of the turbulence, the majority of the results presented in the next section are obtained when the secondary (or scattered) electron population is not taken into account in the electron velocity distribution. This is because the lower level of Landau damping associated with Maxwellian distributions enables a richer dynamics for the turbulence to be observed. The effect of secondary electrons is further discussed in the next section, where a Kappa distribution is included in the total one-dimensional distribution function in order to model the associated energetic tail and enhanced Landau damping.

One final point regarding our simulations that needs to be discussed is the fact that the electron velocity distribution function is kept unchanged throughout the simulation time. It is well known that the distribution function evolves as the electrostatic waves grow in intensity and become intense enough to affect the motions of electrons. In the quasi-linear limit, beam-generated waves ultimately lead to flattening of the positive slope of the distribution function, at which point the transfer of energy from the beam to the waves ceases. For the parameters of electron beams and background plasma used in our simulations (see section 3), the time scale of quasi-linear flattening $\tau_{ql} = \left(\frac{n_0}{n_b}\right)\left(\frac{V_b}{\Delta V_b}\right)^2\omega_p^{-1}$ [*Thurgood and Tsiklauri*, 2015] (where n_0, n_b, V_b, and ΔV_b are the background and the beam electron number densities and the beam mean velocity and velocity spread, respectively) is in the order of tens of milliseconds, which is comparable to time scales, in which the turbulence develops. In such situations, a competition between quasi-linear flattening, replenishment of the positive slope by the streaming electron beam, and additional processes that influence the rate of flattening (such as wave scattering or refraction) determines the amount of energy that is pumped into the turbulence. Investigating such effects is beyond the scope of this work, and proper discussions may be found in a number of previously published works [e.g., *Sanbonmatsu et al.*, 2001; *Krafft et al.*, 2013; *Baumgärtel*, 2014; *Thurgood and Tsiklauri*, 2015]. Assuming that the major effect of evolution of the distribution function and the quasi-linear flattening is to limit the amount of input energy into the system, we believe —for the purpose of this work that focuses on simulating well-developed turbulence that could account for
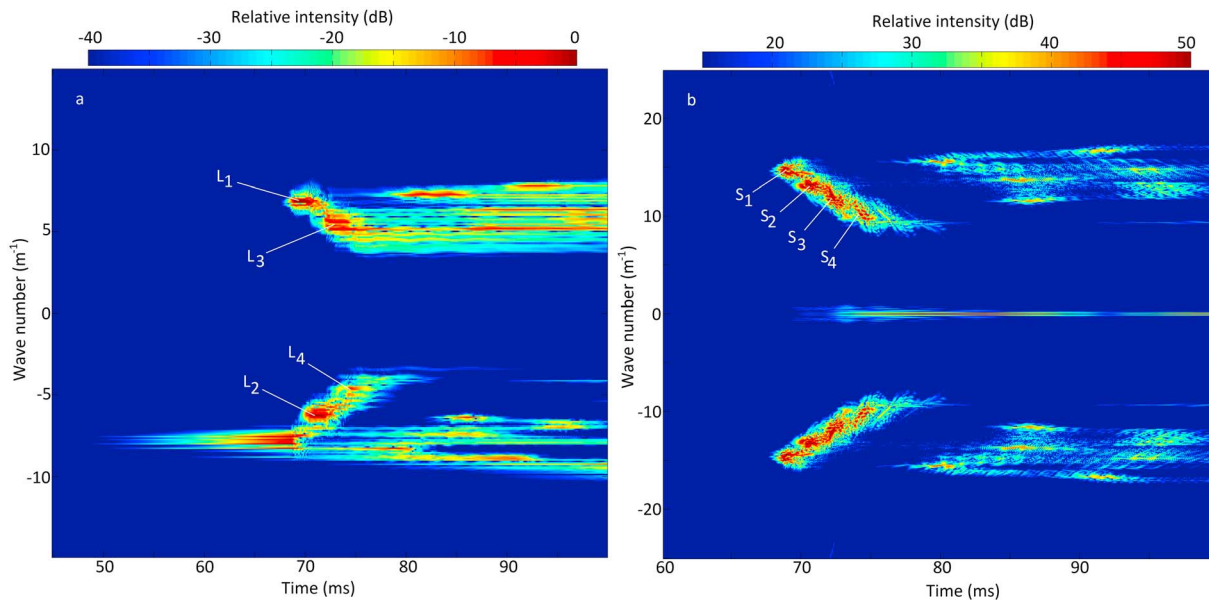
Figure 2. (left and right) The evolution of the electric field and the ion-density perturbations, respectively, as a function of time and wave number for a simulation with the beam parameters of $\frac{n_b}{n_0} = 30 \times 10^{-7}$ and $E_b = 125$ eV applied at time $t = 0$ ms onward.

the ISR observations—that the use of Zakharov equations, which exclude the quasi-linear flattening effect, would still produce insightful results.

Assuming a one-dimensional simulation space of length L with periodic boundary condition, the equations can be solved by the pseudo spectral method [*Guio and Forme*, 2006]. For the simulations we consider a $70 - 100$ m long plasma, time resolution of 0.1 μs, and $N = 2048 - 4096$ spatial Fourier components and apply the one-third zero padding rule to avoid spectral aliasing.

4. Simulations and Discussion

Inputs to the simulator are parameters of the background plasma, as well as parameters of the source electron beams. For the background plasma we consider the typical parameters of the F region peak. These are electron temperature $T_e = 3000$ K, ion temperature $T_i = 1000$ K, electron density $n_0 = 5 \times 10^{11}$ m^{-3}, electron-neutral collision frequency $v_{ec} = 100$ s^{-1}; ion-neutral collision frequency $v_{ic} = 1$ s^{-1}, and we assume that the plasma only consists of atomic oxygen ions. Unless specified, the bulk electron population is considered Maxwellian. As mentioned before, electron beams are modeled by a Doppler-shifted Maxwellian distribution superposed on top of the bulk electron population. In order to capture the whole spectrum of interactions, we considered a wide range of parameters for the electron beams. These are electron number density ratio $10^{-7} \leq \frac{n_b}{n_0} \leq 2.5 \times 10^{-5}$, average beam energy 40 eV $\leq E_b = \frac{1}{2}m_e V_b^2 \leq 2$ keV, and beam velocity spread $\Delta V_b = 0.3\, V_b$; here subscript b indicates *beam*. The upper bound for the average beam energy has been chosen with regard to the fact that the radar echoes are found to be correlated with soft electron precipitations. The lower bound has been chosen with regard to the observation altitudes (~250 km). Precipitating electrons with yet lower energies will be collisionally stopped at higher altitudes and cannot reach to the observation altitudes [*Fang et al.*, 2008]. Below, we present results from a number of simulations that well represent the entire parameter regime that was investigated.

For electron number density ratios $\frac{n_b}{n_0} \sim 10^{-7}$, the growth rate of the resonant Langmuir waves, given by equation (3), is small and the waves do not reach to the nonlinear regime within the 100 ms simulation time. In fact, with such low growth rates, waves would most likely never reach to high intensities, since in the ionosphere and in the presence of background density gradient, propagation of the resonant waves over a longer time period leads to sufficient refraction, which saturates the wave growth due to detuning from the beam [*Akbari et al.*, 2013; *Krafft et al.*, 2013].

As we increase the electron number density ratio, the growth rate increases and the waves may reach to high intensities before the growth is saturated by other processes. Figure 2 shows results of the simulation for one
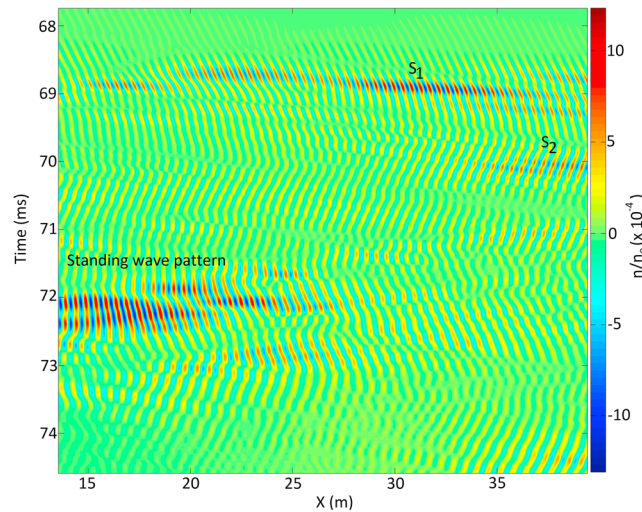
Figure 3. Normalized density fluctuations shown in Figure 2, in real space as a function of time. S_1 and S_2 are the ion-acoustic waves produced by the first and the second PDI in Figure 2.
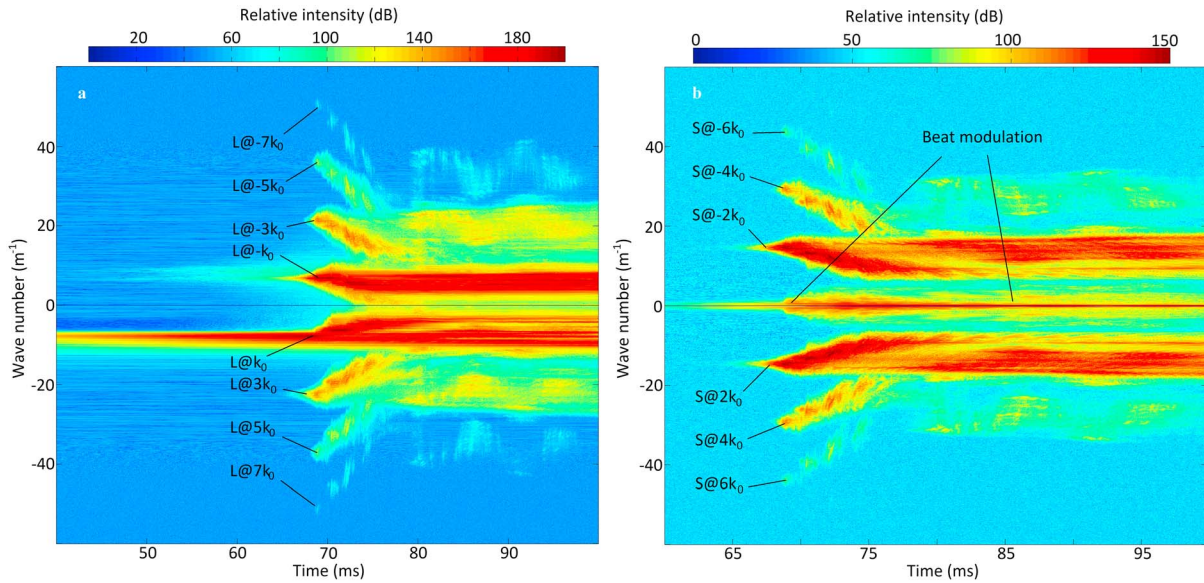
set of beam parameters ($\frac{n_b}{n_0} = 30 \times 10^{-7}$ and $E_b = 125$ eV). Figures 2a and 2b show the evolution of the high-frequency electric field and ion-density perturbations, respectively, as the turbulence evolves in time and wave number. The positive or negative sign of the wave number determines the direction of propagation of the wave. Negative wave numbers correspond to the direction of propagation of the beam. The asymmetric enhancement at $k \sim -8$ m^{-1} for t < 67 ms in the electric field spectrum therefore indicates that only Langmuir waves with wave vector in the direction of the electron beam are initially enhanced. These are the Langmuir waves, for which the damping coefficient ϑ_e is positive due to inverse Landau damping. It can be seen that once the waves with the highest growth rate at $k \sim -8$ m^{-1} reach to high intensities, the PDI is triggered producing counter propagating Langmuir waves (L_1) at $k \sim +7.1$ m^{-1} and ion-acoustic wave (S_1) at $k \sim 15.1$ m^{-1} (in Figure 2b). Soon after the first PDI, the second (L_2, S_2), third (L_3, S_3), and the fourth (L_4, S_4) parametric decays occur and energy quickly transfers to lower wave numbers.

For the plasma parameters used in this simulation we derive $k^* \approx 0.9$ m^{-1} and we verify that the wave number matching conditions $k_s \approx 2k_{L1} - k^*\hat{k}$ and $k_{L2} \approx -k_{L1} + k^*\hat{k}$ are satisfied in Figure 2. In Figure 2b note that since $n(x,t)$ is a real-valued function, its spatial Fourier transform $F(n(x,t))(k,t)$ is a complex function of real wave number k, with even real part, and odd imaginary part, thus even modulus. Therefore, the wave number density spectrum is symmetric with respect to the origin $k = 0$, and the direction of propagation of ion-acoustic waves cannot be distinguished in such wave number density spectrum. Moreover, note that due to strong Landau damping the generated ion-acoustic waves are short lived and damp away shortly after the PDI stops operating at the corresponding wave numbers. This can be seen more clearly in Figure 3, which shows the density fluctuations in real space as a function of time. Here ion-acoustic waves propagating with the sound speed (slope of the patterns in space-time domain) in either directions, as well as a standing wave pattern produced by counter propagating waves, are seen.

In Figure 2b, in addition to the enhancements produced by the parametric decay instability, enhancements at small wave numbers ($k \sim 0$ m^{-1}) are also seen. These are produced by beat modulation between the intense Langmuir waves located close to each other on the Langmuir dispersion curve. Such density enhancements follow their own dispersion relation and will be discussed later. Coalescence-like processes, where Langmuir and ion-acoustic waves merge to produce additional wave activities, are also expected in the presence of strong Langmuir and ion-acoustic waves. Such interactions are secondary compared to the PDI, and thus, the related product waves are not visible in Figure 2 due to the chosen scale for the plot. However, these features are visible in Figure 4, which shows the same data as in Figure 2 but for a broader range of wave numbers and intensities.

In Figure 4a, Langmuir waves at $k_0 \approx -8$ m^{-1} (labeled as $L @ k_0$), Langmuir waves at $k \approx +|k_0|$ (labeled as $L @ -k_0$), and ion-acoustic waves at $k \approx 2k_0$ (labeled as $S @ 2k_0$) are produced by direct interaction with the electron beam and by the parametric decay instability. These are the same waves as in Figure 2. Coalescence of $L @ -k_0$ and $S @ -2k_0$ then produces Langmuir-like enhancements at $k \approx -3k_0$ (labeled as $L @ -3k_0$), which subsequently decay into Langmuir waves at $k \approx k_0$ and ion density waves at $k \approx -4k_0$. The newly generated ion density waves participate in a three-wave coalescence interaction with the most intense Langmuir waves to produce Langmuir-like enhancements at yet higher wave numbers which are, in turn, subject to decay, generating ion density enhancements at yet higher wave numbers. A series of such

Figure 4. The same data as shown in Figure 2 but for a broader range of wave numbers and intensities to illustrate the products of beat modulations and coalescence-like interactions.

interactions ultimately gives rise to the enhancements seen in Figure 4. It is important to note that although the products of the three-wave coalescence and beat modulations are orders of magnitude weaker than the waves produced by the PDI, they are yet orders of magnitude more intense than the background thermal waves. Such interactions might be therefore detectable by incoherent scatter radars.

Figure 5 shows the dispersion relations of the electric field and density perturbations shown in Figure 4. In Figure 4, the $100 - ms$ simulation time is divided into $1 - ms$ periods. Each period is then Fourier transformed with respect to time, and the results for all periods are averaged to produce Figure 5. In Figure 5a, the PDI-generated Langmuir waves, that closely follow the linear dispersion relation $\omega_L^2 = \omega_p^2 + 3k^2 v_e^2$ and waves
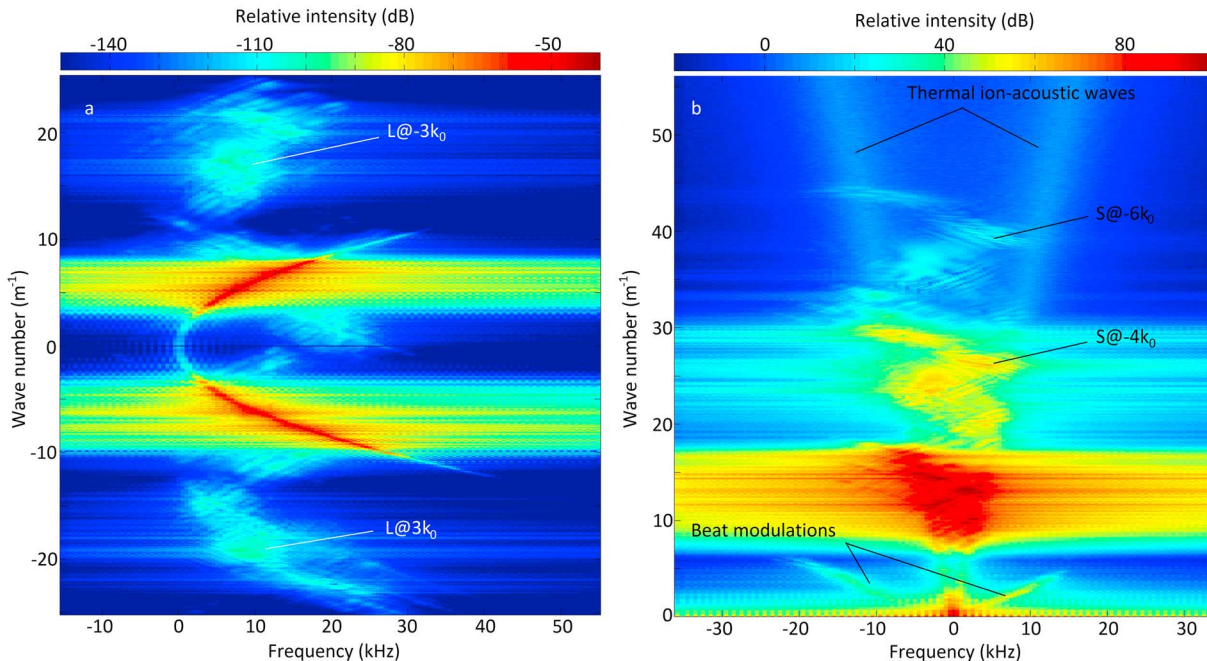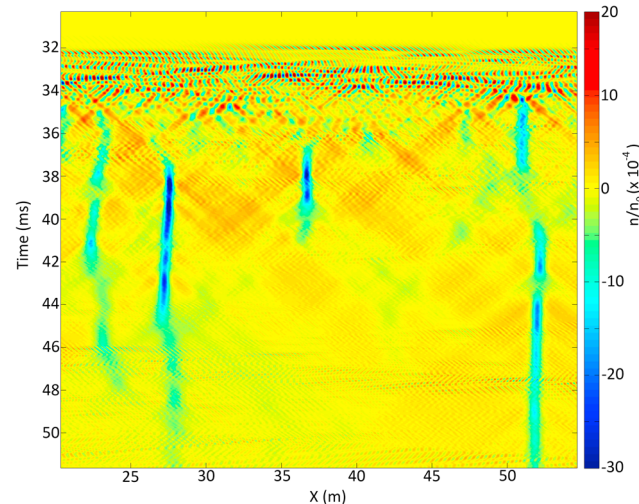

Figure 5. Dispersion relations of the electric field and density perturbations shown in Figure 4. Products waves of the PDI, beat modulations, and coalescence-like interactions are observed.
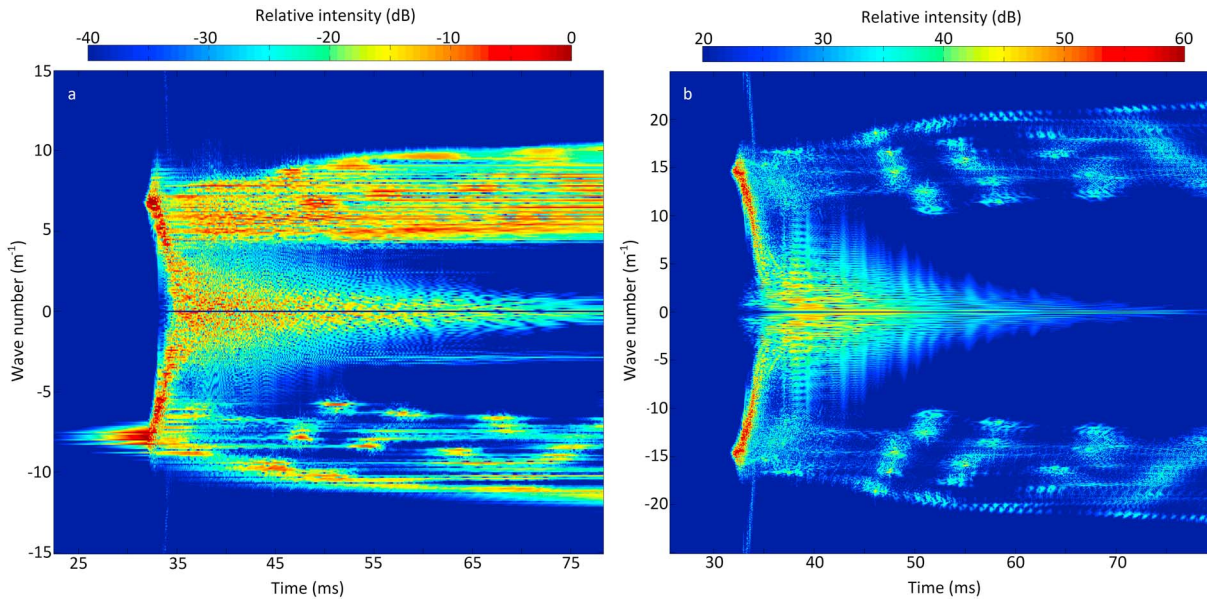
Figure 6. Similar to Figure 2, the left and right plots show the evolution of the electric field and the ion-density perturbations, respectively, as a function of time and wave number for a simulation with the beam parameters of $\frac{n_b}{n_0} = 60 \times 10^{-7}$ and $E_b = 125$ eV applied at time $t = 0$ ms onward.

at higher wave numbers ($L @ 3k_0$ and $L @ -3k_0$) produced by the coalescence-like interactions are seen. Note that the features are downshifted in frequency by an amount equal to the plasma frequency, i.e., zero on the horizontal axis corresponds to $f_p = \frac{\omega_p}{2\pi}$. Ion density perturbations are symmetric with respect to the origin (0, 0) on the frequency-wave number plane; therefore, in Figure 5b we arbitrarily decide to focus on the top half region of the frequency-wave number plane rather than on the right half region. In this case, a horizontal cut through Figure 5b exactly mimics the ion-line spectra that an ISR would measure from the ionospheric plasma. In this figure, the PDI-generated ion-acoustic waves are seen at $8 < k < 18$ m^{-1}. The enhancements at higher wave numbers ($S @ -4k_0$ and $S @ -6k_0$) are those produced by the decay of electric fields transferred to higher wave numbers in Figure 5a. At the highest wave numbers the thermal ion-acoustic waves are seen that follow the linear dispersion relation $\omega^2 = C_s^2 k^2$. Finally, the enhancements at small wave numbers ($k < 8$ m^{-1}) are the density perturbations produced by the beat modulations between Langmuir waves. It can be shown that such enhancements follow the dispersion relation $\omega \approx k \left(3 \frac{v_e^2}{V_b} \right)$ (P. Guio, private communication). In both panels of Figure 5 the horizontal spread of energy from the most intense features are artefacts that appear due to the chosen scale for the plot in order to simultaneously capture features with different levels of intensity.

In Figure 2, the cascades of parametric decay continue until the total electrostatic energy loss, due to Landau damping, equals the energy transfer from the beam to the system. At this point a quasi-steady state is reached. Providing more energy into the system by increasing the beam number density increases
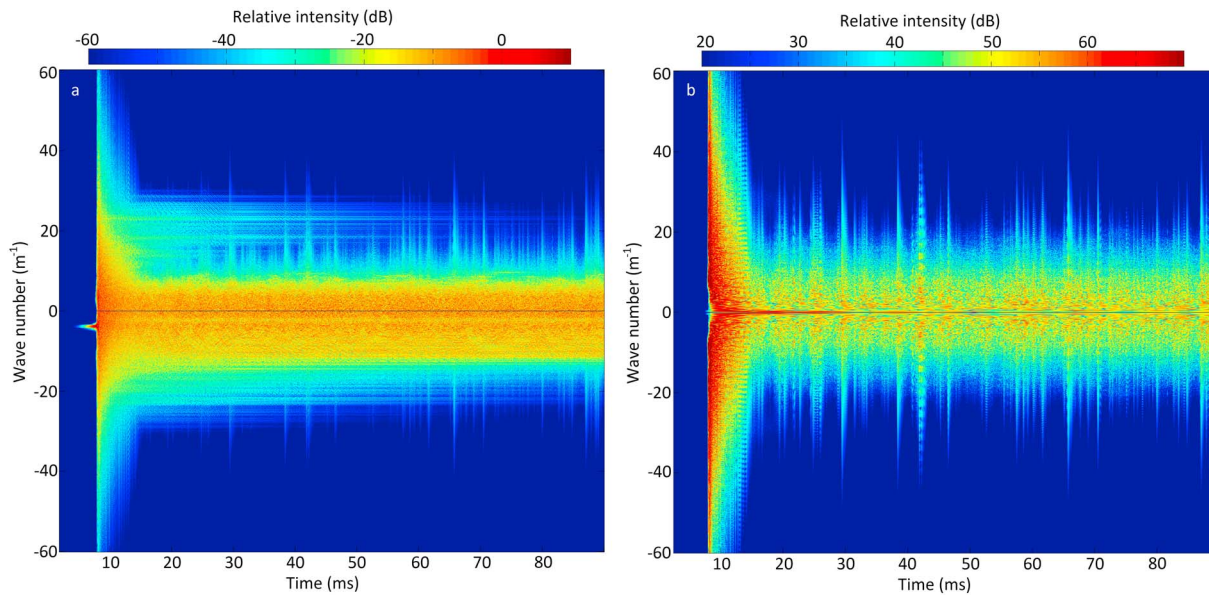

Figure 7. Normalized density fluctuations shown in Figure 6, in real space as a function of time, showing the formation of stationary density cavities following the transfer of energy to the condensate.

Figure 8. Evolution of the turbulence in k space for a simulation with the following electron beam parameters: $\frac{n_b}{n_0} = 150 \times 10^{-7}$ and $E_b = 500$ eV.

the number of cascades and, eventually, energy reaches to the condensate ($k \sim 0$ m^{-1}), where the PDI is prohibited and waves are subject to the modulational instabilities. This scenario has often been mentioned in the literature as one route to caviton formation and wave collapse. Note that transfer of energy to the condensate can also be facilitated by increasing the energy of the beam which, according to the resonance condition $V_b \approx \frac{\omega}{k}$, results in the injection of energy at smaller wave numbers, where the Landau damping is smaller.

Figures 6 and 7 show the results of a simulation for beam parameters $\frac{n_b}{n_0} = 60 \times 10^{-7}$ and $E_b = 125$ eV (the beam electron number density has been increased by a factor of 2 compared to the simulation shown in Figures 2–5). It can be seen that following the first electrostatic decay at $t \approx 32$ ms energy quickly transfers to the condensate, which is characterized in real space by formation of stationary density cavities. In Figure 6a, a portion of Langmuir energy at small wave numbers falls into the modulational, subsonic modulational, and supersonic modulational instability regimes. However, no evident signatures of such instabilities appear.

We next further increase the input energy to the system. Figure 8 shows the evolution of turbulence in k space for the electron beam parameters $\frac{n_b}{n_0} = 150 \times 10^{-7}$ and $E_b = 500$ eV. The first electrostatic decay happens at time $t \approx 8$ ms, after which energy rapidly flows to higher and lower wave numbers. After a few milliseconds the energy at the very high wave numbers dissipates and a quasi-steady state is reached, which is characterized by the concentration of energy at $|k| < 20$ m^{-1} and occasional impulsive energy transfers to higher wave numbers. In Figure 8, the initial stage of the turbulence ($8 < t < 9$ ms) develops extremely fast making it difficult to observe the development in frequency domain. Therefore, in order to capture the frequency domain features at the initial stage we decrease the beam number density to $\frac{n_b}{n_0} = 90 \times 10^{-7}$, which allows a slower development and repeat the simulation. The results are presented in Figure 9.

Figures 9a and 9e correspond to the electric field and density perturbation spectra averaged over the 1 − ms period during which the initial interactions start to appear. Signatures of the initial electrostatic decay are seen on the Langmuir and ion-acoustic dispersion curves (the white dashed lines). During the next 1 − ms period (Figures 9b and 9f) the PDI-generated Langmuir waves intensify and the products of the coalescence-like interactions appear in the electric field spectrum. In the ion density spectrum the enhancement that was located on the dispersion curve, indicating the formation of ion-acoustic waves, now appears at zero frequency, indicating the presence of stationary structures. During the next 1 − ms period (Figures 9c and 9g) it is seen that the energy has covered a broad range of wave numbers and
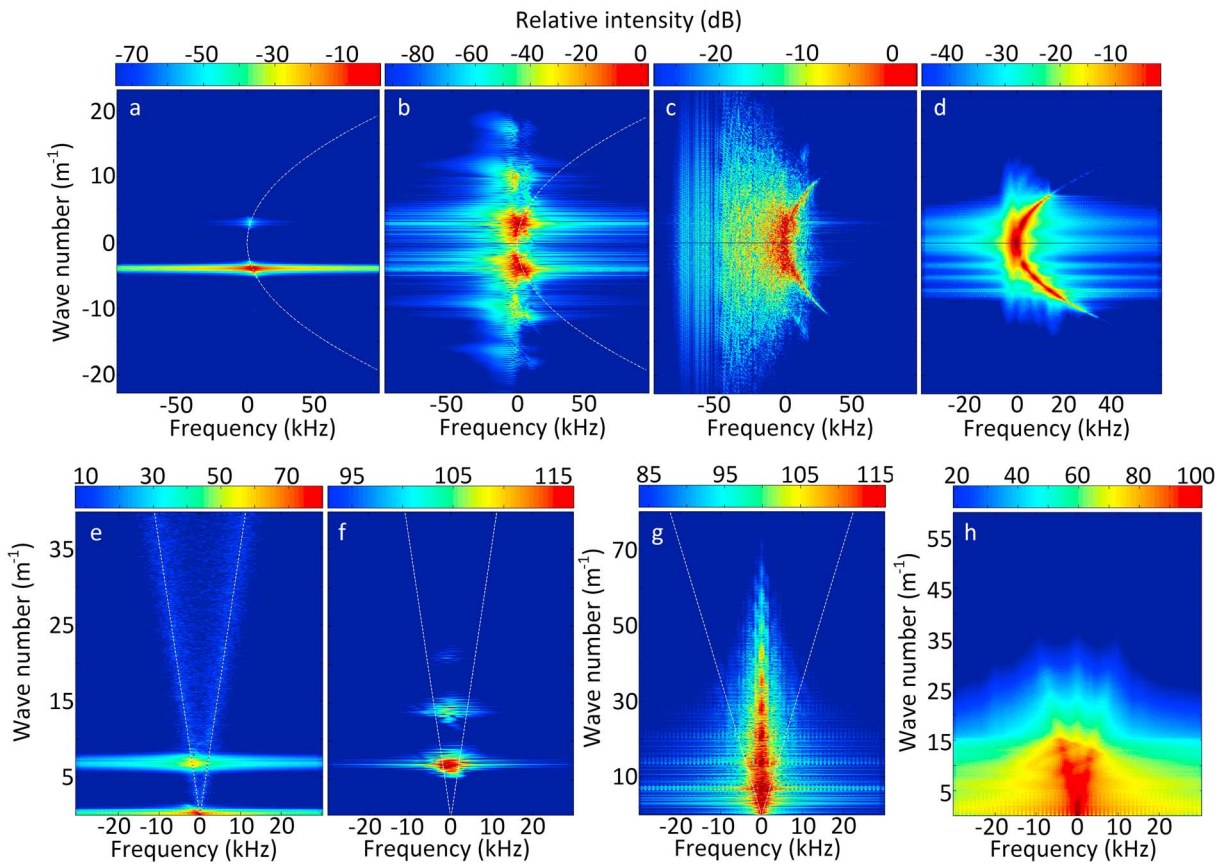
Figure 9. Development of the turbulence (beam parameters $\frac{n_b}{n_0} = 90 \times 10^{-7}$ and $E_b = 500$ eV) in the dispersion relation plane. The top and bottom plots correspond to the electric field and density perturbations, respectively, for four consecutive periods of the turbulence. The dashed white curves are the theoretical dispersion curves for the Langmuir and ion-acoustic waves.

the major portion of the turbulence does not lie on the linear dispersion curves. In the electric field spectrum, in addition to the enhanced Langmuir waves, features appear below the plasma frequency indicating the existence of Langmuir-like fields at regions of low electron density, i.e., density cavities. In the ion density spectrum, zero frequency enhancements appear for a broad range of wave numbers, again indicating the presence of stationary structures. As will be clarified later such spectral features are signatures of caviton formation and wave collapse. Finally, Figures 9d and 9h show the spectral features averaged over a long period once the steady state has reached. Enhanced linear Langmuir and ion-acoustic waves, as well as the signatures of caviton formation as seen in Figures 9c and 9g, although much smoother and less intense, are present.
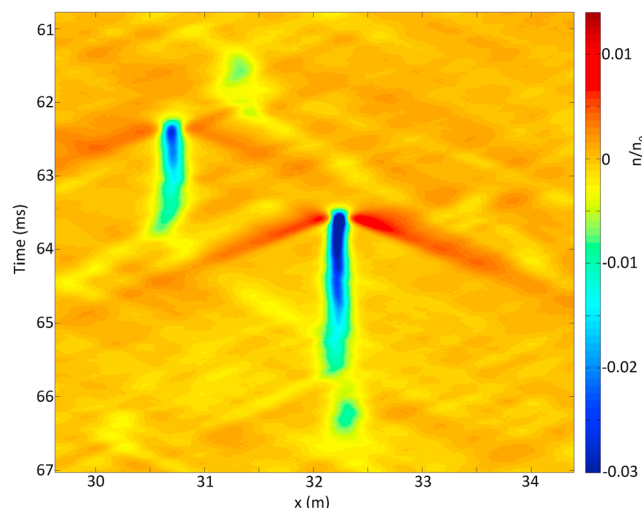
The time evolution of the ion density perturbations in real space is shown in Figure 10. A strong response appears soon after the initial electrostatic decay at time $t \approx 8$ ms. This stage is quickly followed by the formation of narrow, deep, stationary density cavities where the plasma density is up to 10% below the mean background plasma density. Inside the density cavities there exist intense electric fields with amplitudes of up to 40 Vm^{-1} whose ponderomotive force is necessary in order to maintain the density cavities. Such combination of the intense electric field and the associated density cavity is called a caviton. Cavitons have been shown to go through the cycle of nucleation-collapse-dissipation-relaxation [*Doolen et al.*, 1985; *Russell et al.*, 1988; *Robinson et al.*, 1988]. At the start of the cycle and during the nucleation stage, Langmuir energy is trapped (or nucleated) in a density cavity, which may have been generated via stochastic fluctuations in the plasma density. The nucleated Langmuir energy may intensify by accumulating energy from the background turbulence. Once the energy reaches to a threshold, collapse initiates, i.e., the Langmuir energy becomes progressively more intense and the density cavity narrows and deepens as the ponderomotive force further digs the cavity. The extra plasma then propagates to the sides in the form of ion sound pulses. This stage can
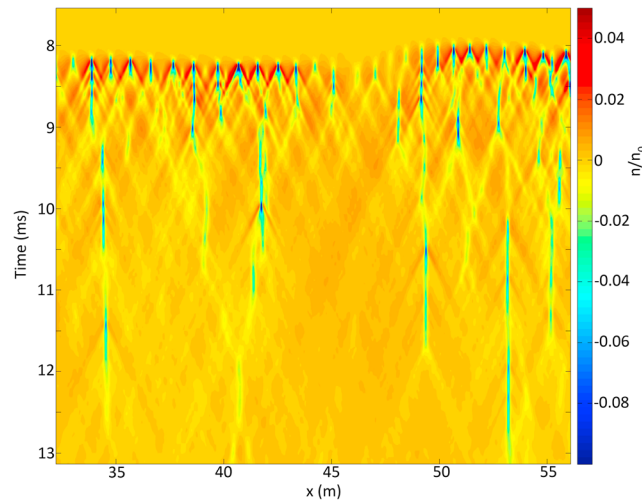
Figure 10. Normalized density fluctuations shown in Figure 8 in real space as a function of time.

be seen in Figure 11, where the formation of a discrete caviton is illustrated. In Figure 8 collapse appears as sudden transfers of energy to high wave numbers (i.e., small spatial scales). At very small scales, tens of Debye length, a combination of linear and nonlinear processes [*Robinson*, 1997, and references therein] dissipates the trapped Langmuir energy. Once a big portion of the Langmuir energy is dissipated the ponderomotive force is no longer high enough to support the deep density cavity. The density cavity, therefore relaxes, shallows and spreads to sides. The remaining shallow density cavities have been shown to be ideal for renucleation of Langmuir energy, which leads to the launch of a new cycle. This is seen in Figure 10 where collocated collapse events happen immediately after the relaxation stage of previous events.

In Figure 10, it can be seen that the initial stage of the turbulence, which is dominated by the formation of many cavitons, is different from the later stage once the quasi-steady state has reached. Moreover, the exact mechanism that leads to the formation of the initial cavitons needs to be clarified. In Figure 12, we revisit the development of the density perturbations (Figure 10) in more details in a logarithmic scale. At $t \approx 8.2$ ms density perturbations are produced as a result of the initial electrostatic decay. We verify that the density structures propagate with the sound speed and that the wavelength of the structure is what that is expected from the parametric decay of the initial Langmuir waves. The propagating ion-acoustic waves are seen to gradually turn into a stationary structure. At this point, every valley of the structure is an ideal location for nucleation and formation of a caviton. This development is consistent with the spectral features observed in Figures 9e–9g. After a few milliseconds the level of density perturbations in the form of ion sound pulses increases due to the burnout of cavitons. The high level of density fluctuations can then disturb the shallow density depressions before they serve as nucleation centers for new cavitons, and thus, the number of cavitons significantly drops after the initial stage.

Figure 11. Normalized density fluctuations in real space as a function of time showing the cycle of nucleation-collapse-dissipation.

Note that the caviton formation at the early stages has dominated the turbulence and prevented any electrostatic decay cascade or modulational instabilities. Figure 13 shows the evolution of the ratio of electrostatic to thermal energy density (W) for the waves with the highest electrostatic energy in the simulation shown in Figures 8, 10, and 12. Initially the Langmuir waves with wave number $k \approx 4$ m^{-1} grow above the thermal level. At the time that the ion density response appears in Figure 12, the Langmuir waves with the highest intensity appear on the boundary of region IV (supersonic MI) and region V (modified decay instability). Yet no signs of supersonic MI or modified decay instability are seen. These results
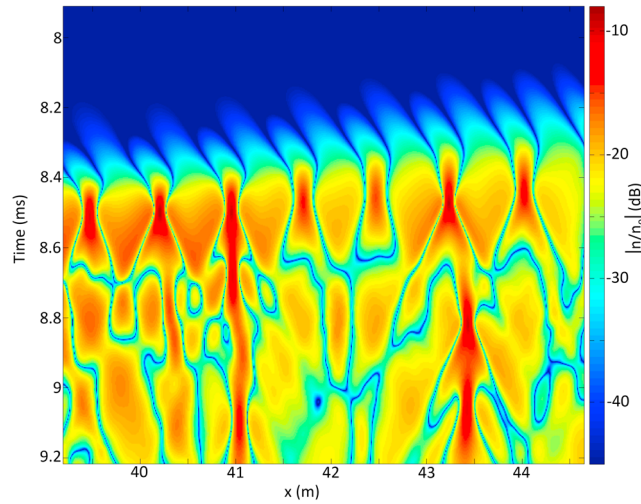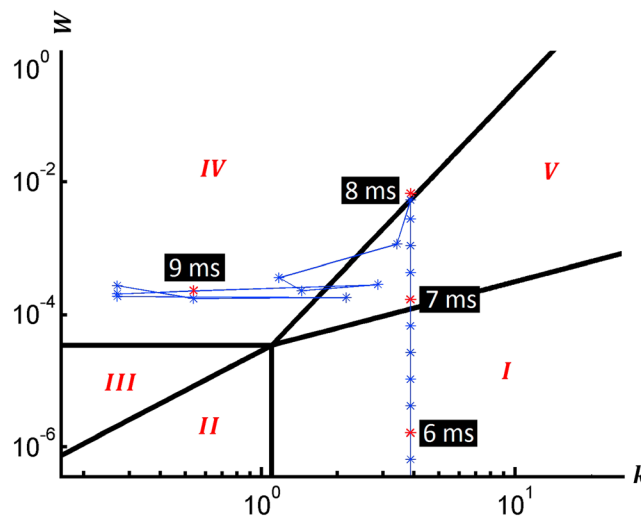
Figure 12. Normalized density fluctuations seen in Figure 10 in logarithmic scale.

are similar to those of *Nicholson and Goldman* [1978], who noted that once the criterion $W > (k\lambda_D)^2$ is satisfied localized packets of waves moving at speeds less than the sound speed would directly lead to collapse and that for such intensities it is not accurate to think of the interactions in terms of the linearized parametric instabilities.

In summary, as we increased the input energy into the system we observed a smooth transition in the dynamics of turbulence from a cascade of PDIs to direct collapse at initial stages. Further increasing the input energy does not significantly alter the initial development of the turbulence and only increases the number of collapse events in the quasi-steady state. However, one should note that upon using much stronger electron beams the validity of the Zakharov equations would soon be under question and the beam-plasma interactions may fall under the control of other processes or higher order nonlinearities, such as electron bunching [*Ergun et al.*, 1991], that cannot be described by the Zakharov equations.

5. The Effect of Secondary (Scattered) Electrons

In the auroral ionosphere, the assumption of pure Maxwellian distribution for the electron gas is often not precise during periods of auroral activity. As a result of primary auroral electrons impinging on the Earth's neutral atmosphere, a secondary electron population with suprathermal energies (a few eV up to ~100 eV) emerges [*Lummerzheim and Lilensten*, 1994]. The total number density of the produced secondary electrons is only a fraction of the number density of the bulk electrons. However, at energies greater than $2 - 3$ eV these secondary electrons dominate the bulk population and generate a power law type tail for the total distribution function. The presence of this energetic tail significantly enhances the Landau damping for Langmuir waves with a range of phase velocities, and as a result significantly alters the dynamics of Langmuir turbulence.

Based on the electron distributions measured with instrument on board sounding rockets, *Newman et al.* [1994a, 1994b] showed that the presence of secondary electrons with the total number density of 4% of the bulk thermal electrons (at the observation altitude of ~700 km) truncates the cascade of parametric decay instability after a few steps and prevents the energy from flowing toward small wave numbers.

Figure 13. Evolution of the electrostatic to thermal energy density (*W*) for the waves with the highest electrostatic energy for the simulation shown in Figures 8, 10, and 12.

In this section, we investigate the effect of secondary electrons on the dynamics of Langmuir turbulence at the *F* region peak. In order to model the secondary electrons, we decide to employ the
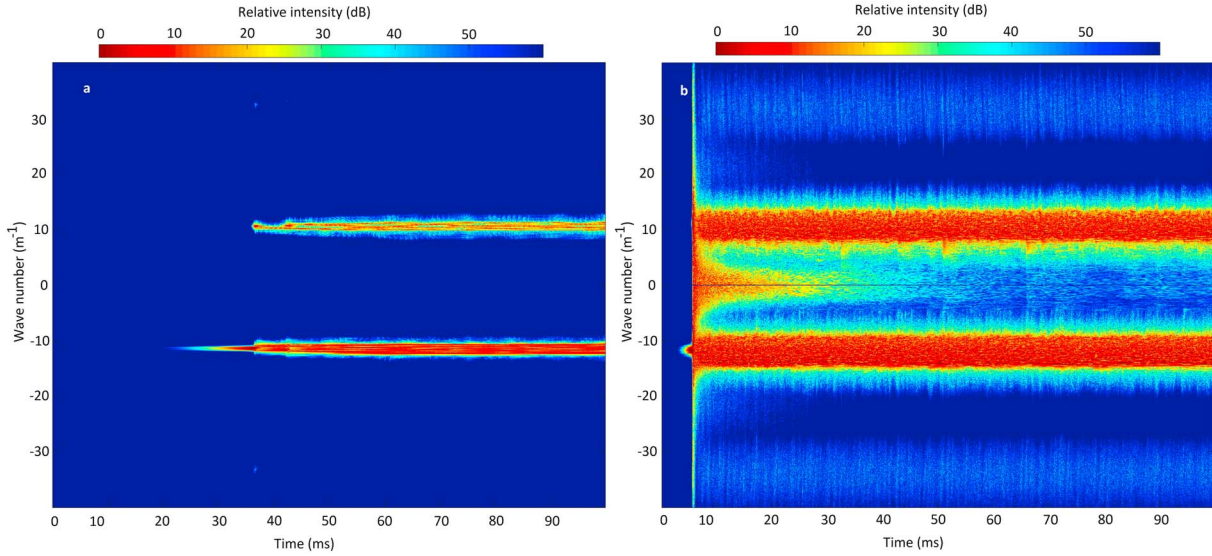
Figure 14. Evolution of the high-frequency electric field (E) in k space for two sets of beam parameters ((left) $\frac{n_b}{n_0} = 4 \times 10^{-5}$, $E_b = 50$ eV and (right) $\frac{n_b}{n_0} = 7 \times 10^{-5}$, $E_b = 50$ eV) once secondary electrons are added to the bulk Maxwellian distribution.

Kappa distribution of *Broughton et al.* [2016] that was determined by fitting the sounding rocket measurements of *Newman et al.* [1994a, 1994b]. The one-dimensional Kappa distribution function is given by

$$f_{\text{Kappa}}(v) = \frac{n_{\text{se}}}{\sqrt{\pi}} \frac{1}{k^{3/2} \, \theta_{\text{se}}} \frac{\Gamma(k+1)}{\Gamma(k-1/2)} \left(1 + \frac{v^2}{k\theta_{\text{se}}^2}\right)^{-k} \tag{6}$$

where n_{se} is the number density of the secondary population, $\theta_{\text{se}} = \sqrt{\left(\frac{k-3/2}{k}\right) \frac{2k_B T_{\text{se}}}{m_e}}$ is the modified thermal velocity, $T_{\text{se}} = 18.2$ eV is the secondary electron population temperature, $k = 1.584$ is the velocity spectral index, and $\Gamma(t) = \int_0^\infty x^{t-1} e^{-x} dx$. We conducted our simulations over a range of secondary electron number densities $\left(0.01\% < \frac{n_{\text{se}}}{n_0} < 1\%\right)$. However, only the results for $\frac{n_{\text{se}}}{n_0} = 0.1\%$, which is a more suitable number at the F region peak [*Maggs and Lotko*, 1981; *Lotko and Maggs*, 1981], are presented. Such low levels of secondary electrons are assumed to have negligible effect on the real part of the plasma dispersion function, and therefore, the dispersion relation of Langmuir waves is assumed to remain unaffected by the secondary electrons.

Figure 14 shows the development of the turbulence (high-frequency electric field as a function of time and wave number) for two sets of beam parameters $\frac{n_b}{n_0} = 4 \times 10^{-5}$ and $E_b = 50$ eV (Figure 14a) and $\frac{n_b}{n_0} = 7 \times 10^{-5}$ and $E_b = 50$ eV (Figure 14b), where a secondary electron population with $\frac{n_{\text{se}}}{n_0} = 0.1$ has been added to the bulk Maxwellian population. For number density ratios $\frac{n_b}{n_0} < 3 \times 10^{-5}$, no parametric decay instability is observed. Therefore, the first obvious effect of the secondary electron population is to significantly increase the minimum beam number density that is required to initiate nonlinear interactions. PDI finally occurs as we increase the beam number density to $n_b = n_0 \times 4 \times 10^{-5}$ (Figure 14a). However, further increasing n_b does not lead to a cascade of PDI or even a secondary PDI. This is in stark contrast to the results previously presented in Figures 2 and 6. As can be seen in Figure 14b, instead of additional PDIs, Langmuir waves produced by the initial PDI grow in intensity, and soon signs of early-stage caviton formation (similar to those in Figure 8) appear. This stage is followed by the broadening of the main Langmuir waves in wave number space, which continues to remain unchanged throughout the simulation. Further increasing the beam number density does not significantly alter the evolution of the turbulence from the results shown in Figure 14b.

6. Summary

In this work we investigated Langmuir turbulence as would be generated in the lower auroral F region by ionospheric electron beams. We investigated a broad range of beam parameters, extending by more than

2 orders of magnitude in average energy and electron number density. As we increased the number density of the electron beam, a smooth transition in dynamics of the turbulence was observed, ranging from a single parametric decay, to a cascade of PDIs, to formation of stationary density cavities in the condensate region, to direct collapse at initial stages of the turbulence.

No definitive signature of modulational instabilities at small wave numbers was seen once the energy reached to the condensate via a cascade of parametric decays. Moreover, no signs of supersonic modulational instability or modified decay instability at high wave numbers were seen once we increased the input energy to the system. Instead, the system quickly moved toward direct formation of cavitons.

The presence of secondary electrons, as modeled by the Kappa distribution, was seen to have a strong weakening effect on the turbulence. Much stronger electron beams are required in order to reach the nonlinear regimes once the secondary electrons are included. Moreover, the enhanced Landau damping introduced by the secondary electrons prevents the turbulence from generating a cascade of PDIs.

Finally, the product waves of coalescence-like interactions, although much weaker than the products of the parametric decay instability, were seen to be orders of magnitude more intense than the thermal-level ion-acoustic and Langmuir waves (see Figures 4 and 5). Such wave enhancements appear at higher wave numbers compared to the beam-resonant Langmuir waves and therefore may be detected by incoherent scatter radars tuned at the proper wave numbers even if the beam-resonant Langmuir waves themselves are invisible to the radar.

References

Akbari, H., J. L. Semeter, H. Dahlgren, M. Diaz, M. Zettergren, A. Strømme, M. J. Nicolls, and C. Heinselman (2012), Anomalous ISR echoes preceding auroral breakup: Evidence for strong Langmuir turbulence, *Geophys. Res. Lett.*, *39*, L03102, doi:10.1029/2011GL050288.

Akbari, H., J. L. Semeter, M. J. Nicolls, M. Broughton, and J. W. LaBelle (2013), Localization of auroral Langmuir turbulence in thin layers, *J. Geophys. Res. Space Physics*, *118*, 3576–3583, doi:10.1002/jgra.50314.

Akbari, H., J. L. Semeter, M. A. Hirsch, P. Guio, and M. J. Nicolls (2015), Evidence for generation of unstable suprathermal electron population in the auroral F region, *Geophys. Res. Lett.*, *42*, 185–192, doi:10.1002/2014GL062598.

Baumgärtel, K. (2014), Ion dynamics in electron beam–plasma interaction: Particle-in-cell simulations, *Ann. Geophys.*, *32*(8), 1025–1033, doi:10.5194/angeo-32-1025-2014.

Bian, N. H., and E. P. Kontar (2011), Parallel electric field amplification by phase mixing of Alfven waves, *Astron. Astrophys.*, *527*, A130, doi:10.1051/0004-6361/201015385.

Broughton, M. C., J. LaBelle, E.-H. Kim, P. H. Yoon, J. R. Johnson, and I. H. Cairns (2016), On the propagation and mode conversion of auroral medium frequency bursts, *J. Geophys. Res. Space Physics*, *121*, 1706–1721, doi:10.1002/2015JA021851.

Diaz, M. A., J. L. Semeter, M. Oppenheim, and M. Zettergren (2010), Analysis of beam plasma instability effects on incoherent scatter spectra, *Ann. Geophys.*, *28*, 2169–2175, doi:10.5194/angeo-28-2169-2010.

Doolen, G. D., D. F. DuBois, and H. A. Rose (1985), Nucleation of solitons in strong Langmuir turbulence, *Phys. Rev. Lett.*, *54*, 804–807, doi:10.1103/PhysRevLett.54.804.

DuBois, D. F., H. A. Rose, and D. Russell (1990), Excitation of strong Langmuir turbulence in plasmas near critical density: Application to HF heating of the ionosphere, *J. Geophys. Res.*, *95*, 21,221–21,272, doi:10.1029/JA095iA12p21221.

DuBois, D. F., A. Hansen, H. A. Rose, and D. Russell (1993), Excitation of strong Langmuir turbulence in the ionosphere: Comparison of theory and observations, *Phys. Fluids B*, *5*(7), 2616–2622, doi:10.1063/1.860699.

Ekeberg, J., G. Wannberg, L. Eliasson, and I. Häggström (2012), Soliton-induced spectrally uniform ion line power enhancements at the ionospheric F region peak, *Earth Planets Space*, *64*, 605–611, doi:10.5047/eps.2012.02.005.

Ergun, R. E., C. W. Carlson, J. P. McFadden, J. H. Clemmons, and M. H. Boehm (1991), Langmuir wave growth and electron bunching: Results from a wave-particle correlator, *J. Geophys. Res.*, *96*, 225–238, doi:10.1029/90JA01596.

Fang, X., C. E. Randall, D. Lummerzheim, S. C. Solomon, M. J. Mills, D. R. Marsh, C. H. Jackman, W. Wang, and G. Lu (2008), Electron impact ionization: A new parameterization for 100 eV to 1 MeV electrons, *J. Geophys. Res.*, *113*, A09311, doi:10.1029/2008JA013384.

Forme, F. R. E. (1993), A new interpretation on the origin of enhanced ion acoustic fluctuations in the upper ionosphere, *Geophys. Res. Lett.*, *20*, 2347–2350, doi:10.1029/93GL02490.

Génot, V., P. Louarn, and D. Le Quéau (1999), A study of the propagation of Alfvén waves in the auroral density cavities, *J. Geophys. Res.*, *104*, 22,649–22,656, doi:10.1029/1999JA900154.

Génot, V., P. Louarn, and F. Mottez (2004), Alfvén wave interaction with inhomogeneous plasmas: Acceleration and energy cascade towards small-scales, *Ann. Geophys.*, *22*(6), 2081–2096, doi:10.5194/angeo-22-2081-2004.

Goldman, M. V., and D. L. Newman (1994), Space-time structure of Langmuir turbulence in the lower solar corona, in *Solar System Plasmas in Space and Time*, edited by J. L. Burch and J. H. Waite, pp. 33–41, AGU, Washington, D. C.

Guio, P., and F. Forme (2006), Zakharov simulations of Langmuir turbulence: Effects on the ion-acoustic waves in incoherent scattering, *Phys. Plasmas*, *13*, 122902, doi:10.1063/1.2402145.

Gurnett, D. A., J. E. Maggs, D. L. Gallagher, W. S. Kurth, and F. L. Scarf (1981), Parametric interaction and spatial collapse of beam-driven Langmuir waves in the solar wind, *J. Geophys. Res.*, *86*, 8833–8841, doi:10.1029/JA086iA10p08833.

Isham, B., C. La Hoz, M. T. Rietveld, T. Hagfors, and T. B. Leyser (1999), Cavitating Langmuir turbulence observed during high-latitude ionospheric wave interaction experiments, *Phys. Rev. Lett.*, *83*, 2576–2579, doi:10.1103/PhysRevLett.83.2576.

Isham, B., M. T. Rietveld, P. Guio, F. R. E. Forme, T. Grydeland, and E. Mjolhus (2012), Cavitating Langmuir turbulence in the terrestrial aurora, *Phys. Rev. Lett.*, *108*, 105003, doi:10.1103/PhysRevLett.108.105003.

Krafft, C., A. S. Volokitin, and V. V. Krasnoselskikh (2013), Interaction of energetic particles with waves in strongly inhomogeneous solar wind plasmas, *Astrophys. J.*, *778*(2), 111, doi:10.1088/0004-637X/778/2/111.

Lotko, W., and J. Maggs (1981), Amplification of electrostatic noise in cyclotron resonance with an adiabatic auroral beam, *J. Geophys. Res.*, *86*, 3449–3458, doi:10.1029/JA086iA05p03449.

Lummerzheim, D., and J. Lilensten (1994), Electron transport and energy degradation in the ionosphere: Evaluation of the numerical solution, comparison with laboratory experiments and auroral observations, *Ann. Geophys.*, *12*, 1039–1051, doi:10.1007/s00585-994-1039-7.

Maggs, J., and W. Lotko (1981), Altitude dependent model of the auroral beam and beam-generated electrostatic noise, *J. Geophys. Res.*, *86*, 3439–3447, doi:10.1029/JA086iA05p03439.

Newman, D. L., M. V. Goldman, R. E. Ergun, and M. H. Boehm (1994a), Langmuir turbulence in the auroral ionosphere 1. linear theory, *J. Geophys. Res.*, *99*, 6367–6376, doi:10.1029/93JA03182.

Newman, D. L., M. V. Goldman, and R. E. Ergun (1994b), Langmuir turbulence in the auroral ionosphere 2. Nonlinear theory and simulations, *J. Geophys. Res.*, *99*, 6377–6391, doi:10.1029/93JA03183.

Nicholson, D. R., M. V. Goldman, P. Hoyng, and J. C. Weatherall (1978), Nonlinear Langmuir waves during Type-III solar radio bursts, *Astrophys. J.*, doi:10.1086/156296.

Nicholson, D. R., and M. V. Goldman (1978), Cascade and collapse of Langmuir waves in two dimensions, *Phys. Fluids*, *21*, 1766–1776, doi:10.1063/1.862093.

Robinson, P. A. (1997), Nonlinear wave collapse and strong turbulence, *Rev. Mod. Phys.*, *69*, 507–573, doi:10.1103/RevModPhys.69.507.

Robinson, P. A., D. L. Newman, and M. V. Goldman (1988), Three dimensional strong Langmuir turbulence and wave collapse, *Phys. Rev. Lett.*, *61*, 702, doi:10.1103/PhysRevLett.61.702.

Robinson, P. A., and D. L. Newman (1989), Quasiperiodic behavior in beam-driven strong Langmuir turbulence, *Phys. Fluids B*, *1*, 2319, doi:10.1063/1.859050.

Robinson, P. A., and D. L. Newman (1991), Strong plasma turbulence in the Earth's electron foreshock, *J. Geophys. Res.*, *96*, 17,733–17,749, doi:10.1029/91JA01734.

Robinson, P. A., D. L. Newman, and A. M. Rubenchik (1992), Effects of long-wavelength dissipation on beam-driven Langmuir turbulence, *Phys. Fluids B*, *4*, 2509, doi:10.1063/1.860166.

Rowland, H. L., J. G. Lyon, and K. Papadopoulos (1981), Strong Langmuir turbulence in one and two dimensions, *Phys. Rev. Lett.*, *46*, 346, doi:10.1103/PhysRevLett.46.346.

Russell, D., D. F. DuBois, and A. R. Harvey (1988), Nucleation in two dimensional Langmuir turbulence, *Phys. Rev. Lett.*, *60*, 581–584, doi:10.1103/PhysRevLett.60.581.

Sanbonmatsu, K. Y., D. L. Newman, and M. V. Goldman (2001), Quasi-linear Zakharov simulations of Langmuir turbulence at rocket altitudes in the auroral ionosphere, *J. Geophys. Res.*, *106*, 10–519, doi:10.1029/2000JA000270.

Schlatter, N. M., N. Ivchenko, T. Sergienko, B. Gustavsson, and B. U. E. Brändström (2013), Enhanced EISCAT UHF backscatter during high-energy auroral electron precipitation, *Ann. Geophys.*, *31*, 1681–1687, doi:10.5194/angeo-31-1681-2013.

Schlatter, N. M., N. Ivchenko, and I. Häggström (2014), On the relation of Langmuir turbulence radar signatures to auroral conditions, *J. Geophys. Res. Space Physics*, *119*, 8499–8511, doi:10.1002/2013JA019457.

Stubbe, P., H. Kohl, and M. T. Rietveld (1992), Langmuir turbulence and ionospheric modification, *J. Geophys. Res.*, *97*, 6285–6297, doi:10.1029/91JA03047.

Thurgood, J. O., and D. Tsiklauri (2015), Self-consistent particle-in-cell simulations of fundamental and harmonic plasma radio emission mechanisms, *Astron. Astrophys.*, *584*, A83, doi:10.1051/0004-6361/201527079.

Tsiklauri, D. (2011), Particle acceleration by circularly and elliptically polarised dispersive Alfven waves in a transversely inhomogeneous plasma in the inertial and kinetic regimes, *Phys. Plasmas*, *18*(9), 092903, doi:10.1063/1.3633531.

Tsiklauri, D. (2012), Three dimensional particle-in-cell simulation of particle acceleration by circularly polarised inertial Alfven waves in a transversely inhomogeneous plasma, *Phys. Plasmas*, *19*(8), 082903, doi:10.1063/1.4745614.

Zakharov, V. E., S. L. Musher, and A. M. Rubenchik (1985), Hamiltonian approach to the description of non-linear plasma phenomena, *Phys. Rep.*, *129*, 285, doi:10.1016/0370-1573(85)90040-7.